Evaluating Large-Eddy Simulation (LES) and High-Speed Particle Image Velocimetry (PIV) with Phase-Invariant Proper Orthogonal Decomposition (POD)

P. Abraham, K. Liu, D. Haworth, D. Reuss, V. Sick

© Photos: DOI: 10.2516/ogst/2013139, IFPEN, X

Dossier

This paper is a part of the hereunder thematic dossier published in OGST Journal, Vol. 69, No. 1, pp. 3-188 and available online here

Cet article fait partie du dossier thématique ci-dessous publié dans la revue OGST, Vol. 69, n°1, pp. 3-188 et téléchargeable ici

DOSSIER Edited by/Sous la direction de : **C. Angelberger**

IFP Energies nouvelles International Conference / Les Rencontres Scientifiques d'IFP Energies nouvelles

LES4ICE 2012 - Large Eddy Simulation for Internal Combustion Engine Flows

LES4ICE 2012 - La simulation aux grandes échelles pour les écoulements dans les moteurs à combustion interne

Oil & Gas Science and Technology – Rev. IFP Energies nouvelles, Vol. 69 (2014), No. 1, pp. 3-188

Oil & Gas Science and Technology – Rev. IFP Energies nouvelles, Vol. 69 (2014), No. 1, pp. 41-59

DOI: 10.2516/ogst/2013126

IFP Energies nouvelles International Conference
Rencontres Scientifiques d'IFP Energies nouvelles

LES4ICE 2012 - Large Eddy Simulation for Internal Combustion Engine Flows
LES4ICE 2012 - La simulation aux grandes échelles pour les écoulements dans les moteurs à combustion interne

Evaluating Large-Eddy Simulation (LES) and High-Speed Particle Image Velocimetry (PIV) with Phase-Invariant Proper Orthogonal Decomposition (POD)

P. Abraham[1], K. Liu[2], D. Haworth[2], D. Reuss[1] and V. Sick[1]*

[1] *University of Michigan, Ann Arbor, MI - USA*
[2] *Pennsylvania State University, University Park, PA - USA*
e-mail: vsick@umich.edu

* Corresponding author

Résumé — Évaluation de données de simulation aux grandes échelles (LES) et de vélocimétrie par imagerie de particules (PIV) via une décomposition orthogonale aux valeurs propres invariante en phase (POD) — Cette étude fait partie d'un programme dont le but est la compréhension des variations stochastiques de l'écoulement des moteurs à combustion interne. En particulier, une comparaison de la vitesse mesurée (PIV) et modélisée (LES) de nombreux cycles du même moteur en marche est présentée. Les procédures de comparaison comprennent une décomposition traditionnelle de Reynolds (vitesse moyenne d'ensemble et RMS) et une POD dépendant de la phase et invariante en phase. La POD dépendant de la phase a été effectuée sur les échantillons PIV et LES de manière séparée et sur les échantillons combinés, créant respectivement des ensembles de modes POD séparés ou combinés. La POD invariante en phase a été effectuée à la fois sur des *snapshots* normalisés et sur des *snapshots* conservant l'énergie initiale.

Des comparaisons initiales des énergies cinétiques spécifiques des vitesses moyennes d'ensemble et RMS ont révélées que les ensembles de données PIV et LES diffèrent de manière significative durant la majeure partie du temps d'admission. Cet écart a d'abord été quantifié en comparant les indices de pertinence calculés entre les champs de vitesse moyenne d'ensemble et, dans un second temps, en utilisant une POD dépendant de la phase, qui a permis de quantifier les variations d'écoulement cycle-à-cycle de la moyenne de Reynolds et de la turbulence. La POD dépendant de la phase a été appliquée séparément pour les ensembles de données PIV et LES durant le temps d'admission (ATDCE, après le point mort haut d'échappement, de 76°), lorsque le jet de la soupape d'admission est intense et que les données PIV et LES diffèrent de manière significative. Il a été estimé que la variabilité cyclique de la moyenne d'ensemble LES est significativement plus élevée que celle de l'ensemble de données PIV. Une POD a aussi été appliquée aux échantillons combinés des *snapshots* LES et PIV afin d'effectuer une comparaison quantitative, créant un ensemble unique de modes et permettant d'effectuer une comparaison uniquement fondée sur les coefficients POD. Des comparaisons ont été effectuées à titre d'exemple pour des données correspondant à une valeur d'ATDCE de 76° et de 330°, représentant une avance d'allumage appropriée pour un moteur à combustion. Les résultats pour l'ATDCE de 76° étaient similaires à ceux obtenus pour l'analyse POD des échantillons séparés. Pour une ATDCE de 330°, les vitesses moyennes d'ensemble et RMS PIV ont présenté une variabilité cyclique légèrement plus élevée.

Une POD invariante en phase a été appliquée aux données combinées de vitesse PIV et LES pour tous les angles de vilebrequin, afin d'étudier l'évolution de l'écoulement en fonction de l'angle de vilebrequin. Les conclusions issues des deux différentes transformations énergétiques sont contrastées. Lorsque l'énergie de chaque champ de vitesse est normalisée, les résultats de la POD invariante en phase sont centrés sur les différences de structure d'écoulement et leur évolution. Par ailleurs, lorsque l'énergie de chaque champs de vitesse est conservée, les résultats de la POD invariante en phase prennent aussi en compte les différences d'énergie entre les données PIV et LES.

Abstract* — *Evaluating Large-Eddy Simulation (LES) and High-Speed Particle Image Velocimetry (PIV) with Phase-Invariant Proper Orthogonal Decomposition (POD) — *This study is part of a program to understand the stochastic variations in IC engine flows; in particular, it is a comparison of measured (PIV) and computed (LES) velocity from multiple cycles of the same motored engine. Comparison procedures included traditional RANS (Reynolds Averaged Navier-Stokes) decomposition (ensemble-averaged and RMS (Root Mean Square) velocity), phase-dependent, and phase-invariant POD. Phase-dependent POD was performed on the PIV and LES samples separately and on the combined samples, thus creating separate or a single POD mode sets, respectively. The phase-invariant POD was performed both on normalized snapshots and on snapshots where the original energy was conserved.*

Initial comparisons of the mass-specific kinetic energies of the ensemble average and RMS velocities revealed that the PIV and LES data sets differed significantly during most of the intake stroke. This discrepancy was quantified first by comparing the relevance indices calculated between ensemble average velocity fields and, second, using phase-dependent POD, which quantified cycle-to-cycle flow variations of the RANS average and turbulence. Phase-dependent POD was applied separately to the PIV and LES data sets during the intake stroke (76° ATDCE, After Top Dead Center Exhaust), where the intake-valve jet is strong and the PIV and LES data were earlier found to be significantly different. The cyclic variability of the LES ensemble average was estimated to be significantly higher than that of the PIV data set. POD was also applied to the combined sample of LES and PIV snapshots for quantitative comparison creating a single set of modes, so that comparison could be made with POD coefficients alone. Example comparisons were made at again for data at 76° and also 330° ATDCE, which is a viable spark timing in a fired engine. The results at 76° ATDCE were similar to those obtained with the POD analysis of the separate samples. At 330° ATDCE, the PIV ensemble average and RMS velocities showed somewhat more cyclic variability.

Phase-invariant POD was applied to the combined PIV and LES velocity data from all crank angles to study the flow evolution over the crank angle range. Conclusions derived from the two different energy transformations are contrasted. When the energy of each velocity field is normalized, the phase-invariant POD results focus on differences in flow structures and their evolution. On the other hand, when the energy of each velocity field is conserved, the phase-invariant POD results also take into account differences in energy between the PIV and LES data.

INTRODUCTION

The traditional Reynolds Averaged Navier-Stokes (RANS) decomposition of flow velocities defines all fluctuations about a mean flow as turbulence. However, in a periodic, unsteady flow such as in an Internal Combustion (IC) engine, varying initial conditions at the start of different cycles, periodically varying boundary conditions throughout the cycle, and the stochastic flow events result in large-scale cycle-to-cycle flow variations, which contribute to the velocity fluctuations but do not necessarily contribute to the traditional concept of turbulence dissipation. Spatial filtering has been used to separate large-scale cyclic flow variations from small-scale turbulence [1-4]. The size of the spatial filters used, or the cut-off frequency, was determined using various metrics, including the temporal autocorrelation function [1], the turbulence power density spectrum [2], the fast-Fourier transforms of the ensemble average velocity [1, 3] and the calculated motion of the flow structures [4]. In [1], the temporal autocorrelation function was used to determine the coherence time of the turbulence (and hence the cut-off frequency) by finding the intercept with zero of the interpolation of the linear decaying zone following

the maximum of the autocorrelation function. This was found to vary with crank angle, engine speed and Laser Doppler Velocimetry (LDV) measurement location. The knee-frequency at the beginning of the region with an f-5/3 slope in the turbulence power density spectrum has also been used as a cut-off frequency [2]. This frequency was also found to vary with crank angle. The fast-Fourier transform of the ensemble average velocity was used to determine the cut-off frequency as the frequency above which the magnitude of the transform approaches zero [1, 3]. The cut-off frequency determined using this method also varies with engine speed and LDV measurement location [1]. However, it was also found that variations of up to ± 100 Hz in the cut-off frequency used result in negligible changes in the turbulence intensities obtained [1]. This is on the same order of magnitude as some of the cut-off frequencies used [3, 4].

In this paper, cyclic flow variations are investigated using Proper Orthogonal Decomposition (POD), which has been used previously to differentiate between cyclic flow variations and turbulence. Baby *et al*. [5] used the first mode to represent the mean in-cylinder velocity. Modes 2-4 are reconstructed to represent the cyclic variability, and the rest of the modes represents the turbulence. Mode 4 was chosen somewhat arbitrarily as the last mode in the truncation by varying the last mode and looking for asymptotic behavior. Cosadia *et al*. [6] found that determining a cut-off mode was not possible, as the cumulative energy fractions of the POD of the instantaneous velocity fields converged very slowly. Chen *et al*. [7, 8] proposed that, if the first mode is a good estimate of the mean flow, the POD coefficients of the first mode may be used to estimate the mass-specific kinetic energy contribution of the mean flow to any velocity field used in the decomposition, thus estimating how closely a particular velocity field compares to the mean flow. Similarly, the mass-specific kinetic energy contribution of all higher modes estimates the RANS turbulence in a specific velocity field. Thus, the cyclic variability of the mean flow and turbulence may be quantified. These studies performed the POD analysis on velocity fields at single crank angles from several cycles (phase-dependent POD).

Additionally, phase-invariant POD has been used to analyze *cyclic variability*, where the coefficients are used to quantify cyclic flow variability [9-12]. In this case, POD is applied to intra-cycle velocity fields from contiguous crank angles and cycles. However, the first mode need not necessarily be the dominant mode at a specific crank angle. Thus, the first mode from a phase-invariant POD analysis cannot be understood as an estimate of the ensemble average flow at all crank angles. Phase-invariant POD has also been used to analyze *in-cylinder flow evolution* [9, 11]. One of its initial applications was the analysis of separate Particle Image Velocimetry (PIV) and Computational Fluid Dynamics (CFD) data sets obtained during the intake and compression strokes of various simplified piston and single valve or intake channel configurations [9]. The results showed the evolution of the tumble vortex formed and its breakdown into small-scale turbulence. A similar phase-invariant POD analysis was used to study the tumble vortex breakdown in the crank angle range of 270° to 360° ATDCE (After Top Dead Center Exhaust) in a more realistic optical engine with a pent roof head and four valves [11]. It was found that the first mode of the phase-invariant POD contained aspects of a large-scale tumble vortex. The coefficients of the first mode then provided an estimate of the dominance of the tumble vortex at various crank angles. As the phase-invariant POD coefficients provide information about both the evolution of flow structures in a cycle and cyclic flow variability, they can provide insight into intra-cycle flow correlations and may be used to find the cause and effect of unusual flow patterns.

In this paper, 60 cycles each of measured (Particle Image Velocimetry, PIV) and computed (Large-Eddy Simulation, LES) velocity data are compared during the intake and compression strokes of a single-cylinder motored optical engine. IC engine simulations have traditionally been performed with RANS decomposition; however, LES is increasingly used as a tool for advanced IC engine design, which explicitly captures the dynamics of the large scales. LES is a bridge between Direct Numerical Simulation (DNS), where all turbulence scales are resolved [10], and RANS, where the effects of all turbulence scales are modeled. Because the statistics of small-scale turbulence are expected to be more universal than those of the large scales, LES offers the promise of more generality and accuracy than RANS with less computational resources than DNS. Compared to RANS, LES is particularly suitable for IC engines because LES is expected to capture more flow structures on the same computational grid and provide better predictive capability with less empirical input required. A key advantage of LES is its capability to study the cycle-to-cycle flow and combustion variations, which are not accessible from RANS [13-16].

Over the last twenty years, significant progress has been made in LES for IC engines. Early reviews of LES applications to IC engines include Celik *et al*. [17] and Haworth [14]. Early LES attempts on IC engines were limited to simple engine configurations; these works include LES for a simplified motored engine configuration by Haworth and Jansen [16], a study of turbulence statistics for a motored engine configuration by Celik *et al*. [18, 19], turbulent premixed-flame propaga-

tion in IC engines on relatively coarse grids by Naitoh *et al*. [20], and LES of Diesel fuel injection and combustion by Smirnov *et al*. [21] and Smith *et al*. [22].

For more realistic configurations, Vermorel *et al*. [23] and Richard *et al*. [24] applied LES with a flame-surface-density-based combustion model (coherent flame model) to a single-cylinder, spark-ignited four-valve engine. Vermorel *et al*. [25] also studied the same engine using LES with a more advanced combustion model (extended coherent flame model). Laget *et al*. [26] performed LES for a four-cylinder engine based on the work of Vermorel *et al*. [23, 25]. The main focus of these works was to estimate cycle-to-cycle variations and to study the root causes for cycle-to-cycle variations in IC engines using a high fidelity LES code. Although only a small number (approximately ten) of engine cycles were simulated in these works, the results showed encouraging qualitative and quantitative agreement with experiments.

Other examples of in-cylinder LES include LES of Diesel engine combustion with CHEMKIN and a flamelet time scale combustion model by Hu *et al*. [27-29], validation of cycle-to-cycle variations for a motored single-cylinder piston engine using LES by Enaux *et al*. [30], LES of Diesel engine combustion with a multi-mode combustion model by Banerjee *et al*. [31] and LES of scalar dissipation rate in an IC engine by Zhang *et al*. [32, 33]. A recent review of LES applications in IC engines by Rutland [34] summarizes the status of this field.

The spatial resolution of LES is comparable to that of PIV. Thus, the data from an LES computation can be analyzed in terms of cyclic flow variations, in a similar manner to experimental data acquired using high-speed PIV. This paper uses more traditional metrics for comparison, such as the ensemble average and RMS velocities, and mass-specific kinetic energies, as well as relevance indices to compare the flow structures in two velocity fields and phase-dependent and phase-invariant POD. Some prior work comparing PIV and LES velocity data has also used phase-dependent POD performed at several crank angles to analyze cyclic flow variations [30]. The ratio between the energy fractions of the first and second modes was used as a measure of cyclic flow variations. The cycle-to-cycle variations in the coefficients of the modes were not considered. Another study by Pera and Angelberger comparing PIV and LES velocity data used just ensemble average and RMS velocities for comparison [35].

In this study, we investigate the use of both the RANS and POD decomposition for comparing measured and computed multi-cycle velocity data. It is part of a larger study of the stochastic flow in IC engines. The LES and PIV data are compared using:

- ensemble averaging and RMS fluctuations,
- phase-dependent POD modes computed for the LES and PIV samples separately,
- phase-dependent POD modes of the combined samples,
- phase invariant POD using two different normalization schemes.

In the following section, the optical engine and high-speed PIV experimental setup is presented, along with a short description of the PIV image analysis procedure. Section 2 presents details of the LES computations, and Section 3 contains the data analysis comparing the PIV and LES data sets. The mass-specific kinetic energies of both data sets are compared as functions of crank angle. Then, ensemble average and RMS velocity fields at four crank angles are compared with each other in terms of relevance indices and mass-specific kinetic energies. Results from a phase-dependent POD analysis of the separate PIV and LES data sets during the intake stroke at 76° ATDCE are presented and a case is made for the phase-dependent POD analysis of a combined PIV and LES data set. It was determined that the first modes from the phase-dependent POD analyses of both the separate and combined data sets were good estimates of the ensemble average velocity fields of the data sets analyzed, allowing for an estimation of the cyclic variability of the ensemble average and RMS velocities. Combined data sets at two different crank angles are analyzed using phase-dependent POD. Finally, phase-invariant POD analyses of combined data sets that have undergone different energy transformations are presented.

1 EXPERIMENTAL SETUP AND PIV DATA ACQUISITION

The optical engine used to collect the PIV data presented in this paper is a two-valve single-cylinder pancake-chamber engine with a simple geometry that was designed to be easily rendered in a Computational Fluid Dynamics (CFD) mesh. The time-resolved velocity and pressure data gathered from this engine are also being used to verify LES engine models developed by collaborators at the University of Wisconsin, Pennsylvania State University, General Motors and Sandia National Laboratories. These data are available upon request. A previous installation of this engine with a quartz ring in the cylinder allowing optical access to only the combustion chamber has been studied [36-38]. Although the present installation of this engine has only been run motored, a spark plug was included in the build so that the in-cylinder flow in its vicinity would be more realistic. The ground strap of the spark plug points towards the

intake valve and is in the plane that bisects the valves. The engine specifications are given Table 1.

Crank angle-resolved pressure data has been obtained at the intake plenum inlet, the exhaust plenum outlet, the interface between the runners from the plenums and the ports in the engine head, and from within the cylinder. For the data presented in this paper, these measurements were used to closely control the pressure boundary conditions to ensure test repeatability.

TABLE 1
Optical engine geometry and valve timings

Bore	92 mm
Stroke	86 mm
Connecting rod length	231 mm
Crank radius	43 mm
Geometric compression ratio	10:1
Displacement	0.57 L
Clearance volume	0.064 L
Intake valve opening	0° ATDCE
Intake valve peak lift	114° ATDCE
Intake valve closing	229° ATDCE
Exhaust valve opening	494° ATDCE
Exhaust valve peak lift	606° ATDCE
Exhaust valve closing	720° ATDCE

The intake and exhaust system pressures, engine speed data, and peak cylinder pressures from the 60 PIV cycles under consideration were examined to determine if there were any significant cycle-to-cycle variations in engine operation parameters and boundary conditions and to ensure that the engine operating conditions matched those used for the LES calculations. Table 2 details the measured average engine parameters and their standard deviations.

The standard deviations of the pressures measured in the intake and exhaust systems given in Table 2 are well within the ± 0.03 kPa precision error associated with the transducers used. The rpm variations were found to be within ± 1 rpm of the mean. The standard deviation in the surface temperature of the quartz cylinder was less than the ± 1.1°C error associated with the thermocouple wire used in this setup. Thus, it expected that these minimal variations in boundary conditions would not significantly influence in-cylinder velocities. The difference between the maximum and minimum peak cylinder pressures was found to be 0.8% of the average peak cylinder pressure.

The laser used in these experiments is a high repetition rate frequency-doubled Q-switched dual-cavity diode-pumped Nd:YLF laser (*Quantronix*, Darwin-Duo). The laser sheet created had a thickness of 2 mm and was placed in the tumble plane bisecting the valves and containing the spark plug ground strap. The camera used in these experiments is a high-speed camera with a CMOS sensor (*Vision Research*, Phantom v7.3). It has a dynamic range of 14 bits, a pixel size of 22 μm, and a full sensor resolution of 800 × 600 pixels. A 210 mm focal length camera lens (*Nikon* Micro-Nikkor

TABLE 2
Measured engine parameters

Engine parameter	Test average	Standard deviation
Engine speed	799.4 rpm	0.22 rpm
Air temperature at intake port	45.6°C	0.00°C
Pressure at intake plenum inlet	95.0 kPaA	0.0058 kPaA
Intake port pressure	94.6 kPaA	0.0059 kPaA
Exhaust port pressure	101.5 kPaA	0.0069 kPaA
Pressure at exhaust plenum outlet	101.4 kPaA	0.0069 kPaA
Peak cylinder pressure	1910.2 kPaA	2.74 kPaA
Oil temperature at inlet	40.3°C	0.04°C
Coolant temperature at outlet	39.5°C	0.00°C
Cylinder surface temperature	44.9°C	0.18°C

210 mm ED) was used to minimize parallax errors. The intake air flow was seeded with silicone oil droplets with a nominal diameter of 1 μm.

The PIV data presented in this paper was taken at full camera resolution every 2° from 2° to 360° ATDCE for 60 consecutive cycles. The field-of-view of the camera included the entire illuminated tumble plane from the piston at BDC to the engine head. The magnification was 0.163. The camera lens aperture was set to f/4 to ensure that sufficient light reached the camera sensor while maintaining adequate depth-of-focus settings. The time difference between laser pulses, dt, was 10 μs. This improves the accuracy of the large intake jet velocities by limiting the maximum particle image displacement in the intake jet to 8 pixels and lowering particle loss from the light sheet between PIV image pairs. However, this short time difference between image pairs leads to low velocity resolution, which is insufficient towards TDC compression when velocities are low. It is not possible to accurately resolve velocities smaller than that associated with the 0.1 pixel uncertainty in the resolution of particle displacements [39]. In this case, the smallest velocity that can be accurately resolved is 1.35 m/s.

A sliding minimum subtraction was carried out to improve the signal-to-noise ratio of the raw PIV images. Then, velocity vectors were calculated using a multi-pass PIV algorithm employing interrogation windows of decreasing size (128 × 128 pixels to 32 × 32 pixels) with a 50% overlap. This results in a spatial resolution of 4.33 mm with a separation between velocity vectors of 2.16 mm. Some vector post-processing was performed. Vectors with a correlation peak ratio less than 1.4 were deleted. A median filter was applied, and interpolation was used to fill in vectors.

2 LES COMPUTATIONS

LES data from the intake and compression strokes of 60 consecutive cycles is presented in this paper for the same crank angles where PIV data was taken, *i.e.*, every 2° from 2° to 360° ATDCE. The simulations were run through 70 consecutive engine cycles but the first 10 cycles were discarded to avoid contamination by initial conditions. A commercial finite-volume CFD code (*CD-Adapco*, STAR-CD version 4) [40, 41], has been used for this study. A second-order differencing scheme (monotone advection and reconstruction scheme, MARS [42]) was used for the convective terms in the momentum equation, and the PISO algorithm [43, 44] was used for pressure-velocity coupling, which results in a temporal accuracy comparable to a second-order scheme. A one-equation model for the sub-grid scale, with a modeled transport equation for sub-grid scale turbulent kinetic energy, was solved [45]. The sub-grid scale turbulent kinetic energy was then used as a velocity scale for the sub-grid viscosity [46]. A third-order Spalding law [47] was applied as the wall model. More details of the near-wall treatment and other aspects of the LES computations can be found in [48].

The computational domain includes the in-cylinder region, ports, runners, and plenums. The port-and-cylinder mesh topology is shown in Figure 1.

The unstructured hexahedral mesh was generated using es-ice [49]. Non-aligned interfaces were applied in the extrusion layer close to the boundary layer. During the piston movement, in-cylinder cell layers (horizontal slices) were deleted and added in the axial direction without changing the mesh topology. The deletion layer was set at a fixed number of layers above the highest bottom face. Similar treatments were also applied for the valve movements. The mesh has approximately 700 000 cells including the plenums at Bottom-Dead Center (BDC) and approximately 500 000 cells at TDC; most of the in-cylinder cell dimensions range between 1 mm and 1.2 mm. This relatively coarse mesh has been used to facilitate runs through large numbers of consecutive engine cycles. The mesh size in the vicinity of the spark-plug and valves (approximately 0.4 mm cells) was somewhat smaller in size to better capture those geometric features. The computational time step was 0.1 Crank Angle Degrees (CAD) through most of the engine cycle, although somewhat smaller time steps were used during valve opening and closing. As discussed in [14, 16, 34, 48], earlier in-cylinder LES studies showed that approximately 80% of the turbulence kinetic energy is captured for meshes comparable to those that have been used here.

The working fluid in these simulations was air, which was treated as an ideal gas, and the initial temperature in the cylinder and plenums was 318.16 K. The initial pressures in the cylinder and outlet plenum were 101.500 kPaA, and 95.000 kPaA in the inlet plenum. No-slip boundary conditions with wall functions were applied at solid walls, and the wall temperature was fixed at 318.16 K during the computation. Time-varying pressure and temperature boundary condition were applied at the plenum inlets/outlets. These boundary conditions were obtained from the 1-D simulation results using GT-Power, without any cycle-to-cycle variations.

3 COMPARING PIV AND LES DATA

Comparison of LES and PIV data requires the samples be on a common grid. As both the resolution and spatial

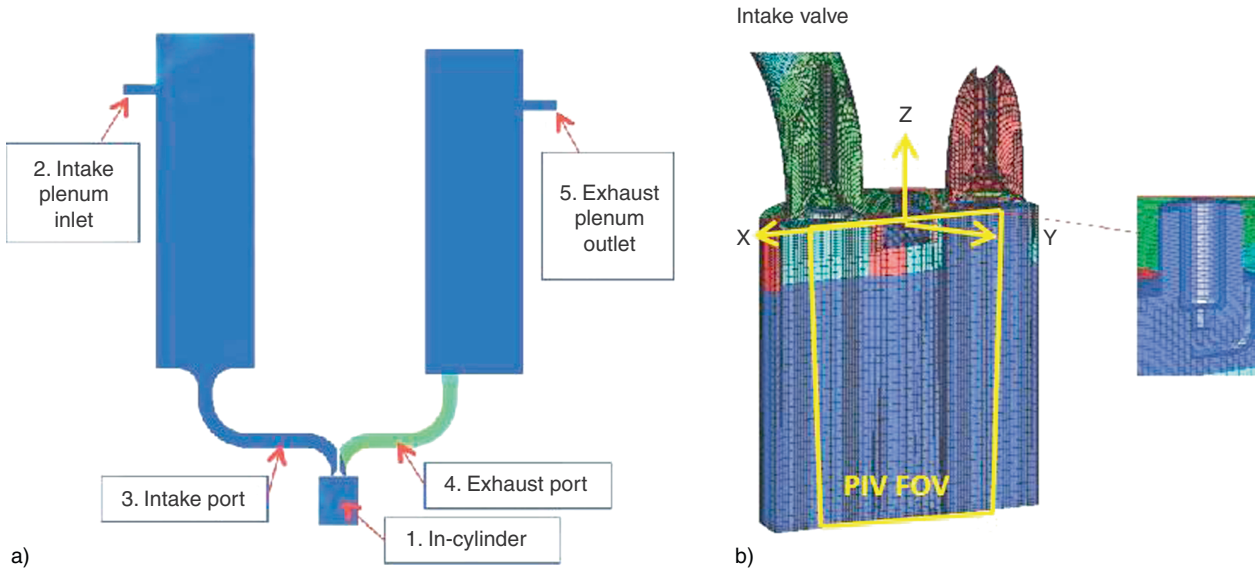

Figure 1

a) Computational domain for LES of the TCC engine. The locations of five monitoring points are shown. b) Plane in which PIV data was acquired (tumble plane bisecting the valves and containing the spark plug).

extent of the LES data is different from that of the PIV data, the LES data was interpolated onto the respective PIV grid at each crank angle. It is this interpolated LES data that has been used in the all of the following comparative analyses.

3.1 Ensemble Average and RMS Energies and Velocities

As a first comparison between the PIV and LES data sets, the mass-specific kinetic energies of the ensemble average and RMS velocities of each data set were computed at each crank angle. Figure 2 plots the kinetic energies of the ensemble average velocities, with error bars whose length equals the kinetic energies of the RMS velocities, as a function of crank angle. The kinetic energies shown here were determined form the in-plane velocity components because only those were measured in the PIV experiments.

Figure 2 shows that the largest difference between the PIV and LES ensemble average energies occurs at approximately 60° ATDC, where the LES energy is 40% higher and 160° ATDCE, where the PIV is twice as large. The RMS kinetic energies of the PIV and LES data sets also differ over most of the intake stroke.

A more detailed comparison between the LES and PIV data sets at the three crank angles are given in Figure 3 and Table 3, which present the ensemble average and RMS velocity vector fields and the total mass-specific kinetic energy, respectively. Figure 3 also contains the relevance indices between the ensemble average velocity fields from the two data sets. The relevance index, $RI_{U,V}$, is the metric chosen to quantify the equivalence of structures present in two different velocity vector fields U and V. It is computed by projecting one velocity field onto another and is defined as follows:

$$RI_{U,V} = \frac{(U,V)}{||U||.||V||} \tag{1}$$

In Equation (1), the numerator is the inner product of two velocity fields over the whole domain. If U and V are identical, $RI_{U,V}$ will be equal to 1. If $RI_{U,V}$ is equal to -1, U and V are exactly opposite. U and V are orthogonal if $RI_{U,V}$ is equal to 0 [9].

As is to be expected from Figure 2, Figure 3 shows that the PIV and LES ensemble average velocities at 76° ATDCE during the intake stroke are dominated by the jet through the intake valve. The largest difference between the ensemble averages is in the lower left of the grid where the vectors in the LES ensemble average are larger and directed to the upper left, whereas a vortex structure with smaller velocities is seen in the PIV ensemble average. The RMS velocities at 76° ATDCE also show that, outside of the intake jet region close to the intake valve, the LES data set has larger fluctuations about the ensemble average velocities.

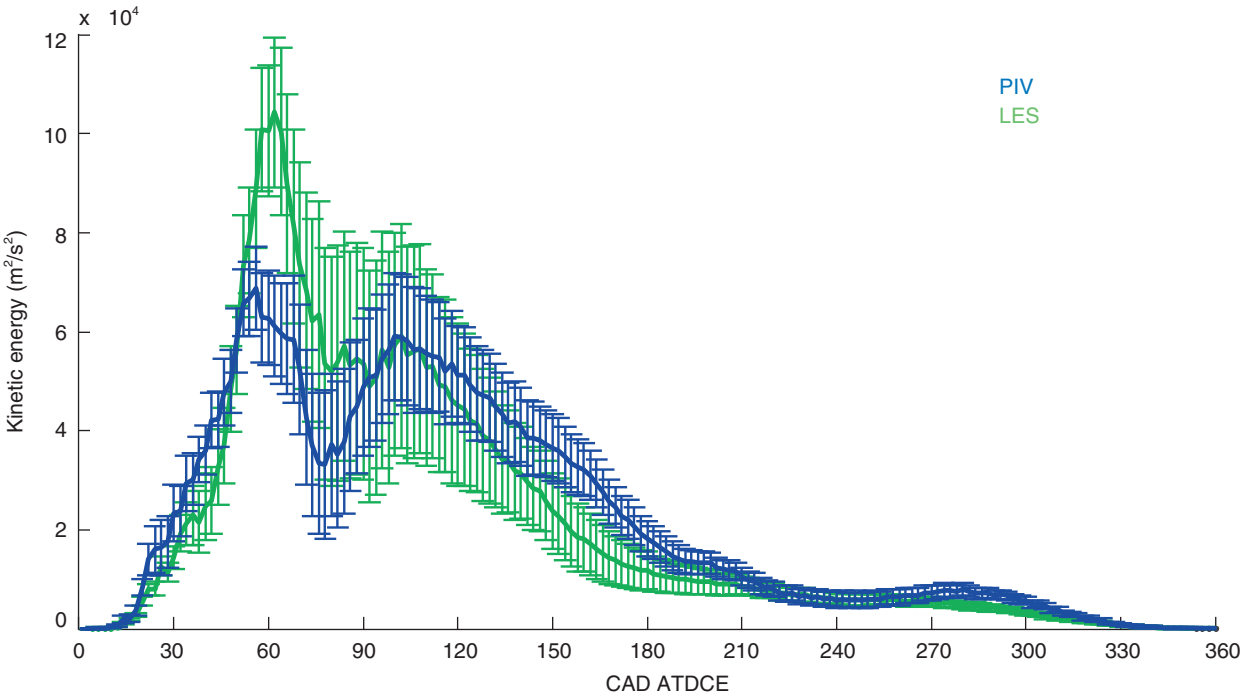

Figure 2

Kinetic energy of the ensemble average velocities (solid lines) and kinetic energy of the RMS velocities (error bars) during the intake and compression strokes.

At 250° ATDCE, just after intake valve closing, the LES ensemble average shows that the large-scale tumble structure formed during the intake stroke persists to the early part of the compression stroke. However, the tumble vortex center is no longer visible in the field-of-view in the PIV ensemble average, perhaps having rotated out of plane or shifted to the right. The LES RMS velocities at 250° ATDCE are significantly smaller than those of the PIV data set. Although the relevance indices between the PIV and LES ensemble average velocities all indicate significant dissimilarities in velocity structures, the relevance index between the ensemble averages is lowest at 250° ATDCE, quantitatively indicating that they are most dissimilar in terms of velocity features at this crank angle. Recall from Figure 3 and Table 3 that 250° ATDCE is when the total mass-specific kinetic energies of the ensemble average velocity fields were most similar. This indicates the importance of comparing both kinetic energies and relevance indices to quantify the equivalence of PIV and LES results.

At 330° ATDCE, which is a viable spark timing, the LES flow shows remnants of the tumble not visible in the PIV measurements. Here, the differences between the ensemble average velocities of the PIV and LES data are captured by both the relevance index value and the difference in kinetic energy.

This section illustrates that the flow measured and computed in the sampled plane are different in appearance. This of course could be due to a swirl component to the flow creating an out-of-plane motion that moves otherwise similar structures out of the cutting plane. Regardless of the reason for the differences, this section demonstrated that a combination of the kinetic energy and relevance index can quantify the differences, and that both are necessary to capture the differences.

3.2 Phase-Dependent POD: Separate Data Sets

Here, the similarities of the LES and PIV fields are analyzed using phase-dependent POD, where the POD is performed on samples from a fixed crank angle but performed separately on the computed and measured samples. Thus, the sampling is identical to that employed when ensemble averaging as shown above. To demonstrate the attributes of this technique, phase-dependent POD was used to analyze snapshots at 76° ATDCE from 60 consecutive cycles from PIV and LES, respectively. Previous studies [7, 8] have shown that the first mode

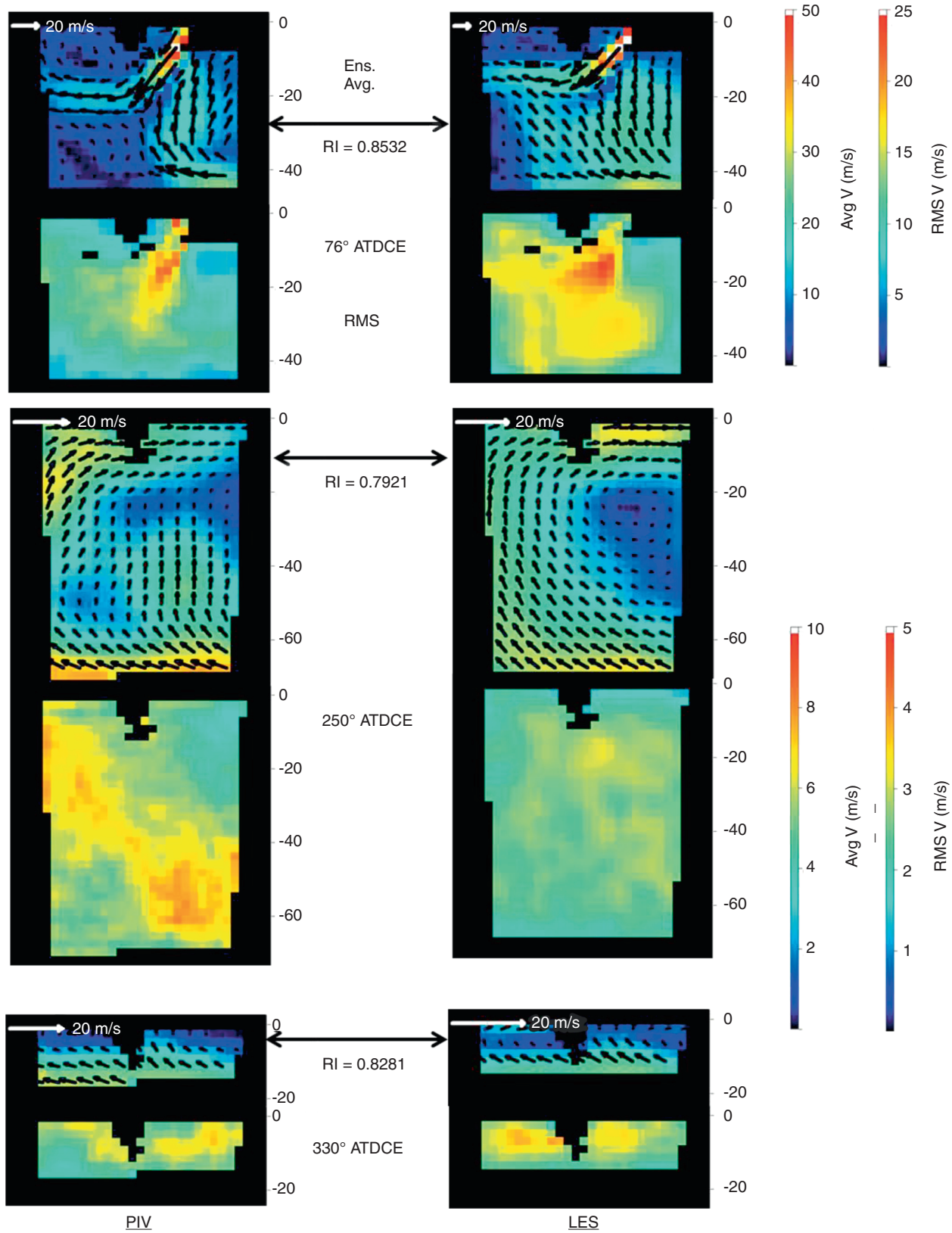

Figure 3

Measured and computed ensemble-average (every second vector shown) and RMS velocity distributions.

TABLE 3
Measured and computed ensemble-average and RMS kinetic energies

	Kinetic energy of ensemble average (m^2/s^2)		Kinetic energy of RMS (m^2/s^2)	
CAD ATDCE	PIV	LES	PIV	LES
76	33 470	63 420	28 640	45 630
250	5 859	5 755	3 169	2 220
330	948	623	548	554

from a phase-dependent POD analysis can be an excellent low-order estimate of the ensemble average. Figure 4 verifies this statement for the two data sets examined here by comparing mode 1 from each analysis to the ensemble average of the input data set using the relevance index and mass-specific kinetic energies.

Figure 4 shows the pattern similarity and the near-unity magnitude of the relevance indices of mode 1 and the ensemble averages of both the PIV and LES data, respectively. Further, the differences between the average mass-specific kinetic energies of the PIV and LES first modes and the ensemble average kinetic energies of the PIV and LES data sets are small, indicating that mode 1 is a good estimate of the ensemble average velocity for both data sets. It is worth noting here that the sign of the velocity components in a mode does not necessarily reflect the direction of a flow structure. For example, in Figure 4 it is apparent that the dominant flow structure past the intake valve shows up in reverse in mode 1. As a result, the relevance index between this mode and the ensemble average flow field will be negative.

The differences between the average mass-specific kinetic energies of the PIV and LES modes 2 through M (the total number of modes) and the RMS average kinetic energies of the PIV and LES data sets are also small, indicating that the energies of modes 2 through M together form a good estimate of the RMS average velocity for both data sets. Thus, as in previous work [7, 8], the mass-specific kinetic energy contribution of mode 1 in each snapshot is a good measure of its RANS ensemble average content, and the mass-specific kinetic energy contribution of modes 2 through M in each snapshot is a good measure of its the RANS turbulence content. The mass-specific kinetic energy contribution of a particular mode m to a snapshot k ($ke_{m,k}$) is calculated from the POD coefficient c_m^k as follows:

$$ke_{m,k} = \frac{1}{2}\left(c_m^k\right)^2 \tag{2}$$

Thus, it is possible to estimate the ensemble-average energy in a given cycle (snapshot) as:

$$ke_{1,k} = \frac{1}{2}\left(c_1^k\right)^2 \tag{3}$$

and the turbulence by summing coefficients of that cycle from modes $2 \rightarrow M$.

In using this measure, Figure 5 shows the cyclic variability of the RANS ensemble average and RANS turbulence *via* the mass-specific kinetic energy contributions of mode 1 and modes 2 through M to instantaneous snapshots at 76° ATDCE for both the PIV and LES data sets.

Figure 5 shows that the range of mode 1's kinetic energy contribution for the LES data set is over twice that for the PIV data set. This illustrates that the cyclic variability of the LES ensemble average kinetic energy is higher than that of the PIV ensemble average kinetic energy. The cyclic variability of the RANS turbulence is similar for both data sets at this crank angle. In fact, the cyclic variability of both the ensemble average kinetic energy and the RANS turbulent kinetic energy are of a similar magnitude for the PIV data set. Thus, it is possible to quantify the cyclic variability of the RANS ensemble average and RANS turbulence.

Similar to Figure 3, the relevance index between the first mode from the PIV data and LES data phase-dependent POD analyses is 0.8336, indicating that they are not very similar to each other. Thus, it is not possible to quantify the kinetic energy differences between the measured and computed flows beyond what was possible with the traditional analysis in Section 3.1.

3.3 Phase-Dependent POD: Combined Data Set

Here the equivalence of the LES and PIV fields are analyzed using phase-depended POD, where the POD is performed on combined samples from a fixed crank angle. To demonstrate the attributes of this technique phase-dependent POD on the combined samples was applied at 76° ATDCE, during the intake jet, and 330° ATDCE, a viable spark timing in a firing engine. This yields a single set of modes at each crank angle. Thus, the coefficients may be subsampled by their association with

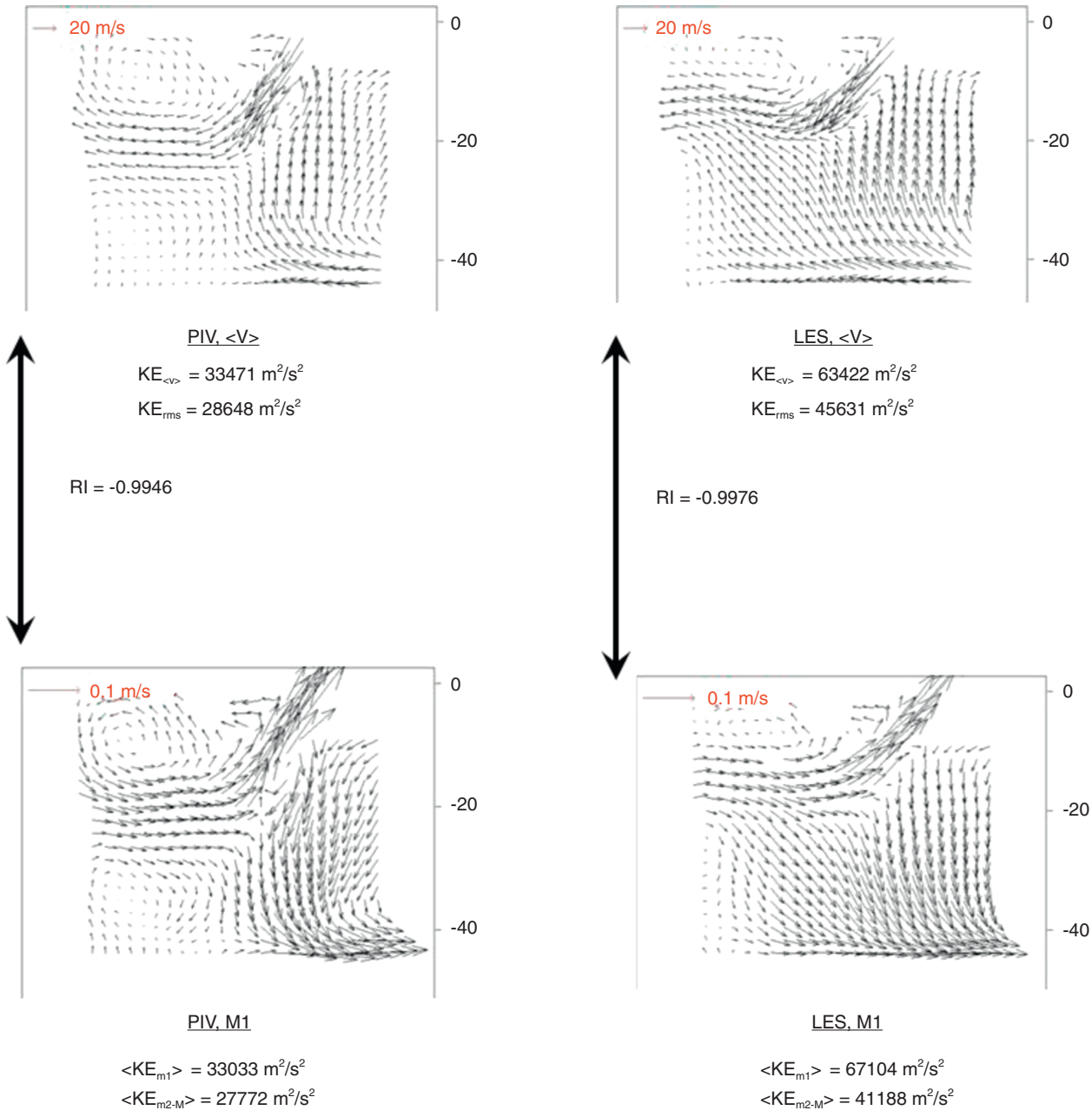

Figure 4

Example of phase-dependent POD mode 1 as an excellent estimate of the ensemble average, based on the relevance index, *RI*, and the kinetic energy, *KE*. The POD analysis was performed on the LES and PIV samples separately using data at 76° ATDCE.

either PIV or LES snapshots, and the kinetic energy contributions of different modes to different snapshots may be directly compared for both the PIV and LES data.

Table 4 provides a comparison of the mass-specific kinetic energy and relevance indices at 76° ATDCE. Mode 1 is a good estimate of the ensemble average of both the PIV and LES data sets (though the LES Mode1 is a somewhat better estimate) as the kinetic energies associated with the RANS ensemble average velocity field and the average energy contributed by mode 1 of the combined data set to the PIV and LES snapshots compare well with each other and the relevance indices between mode 1 and the ensemble averages are high. Table 4 also shows that the total kinetic energy

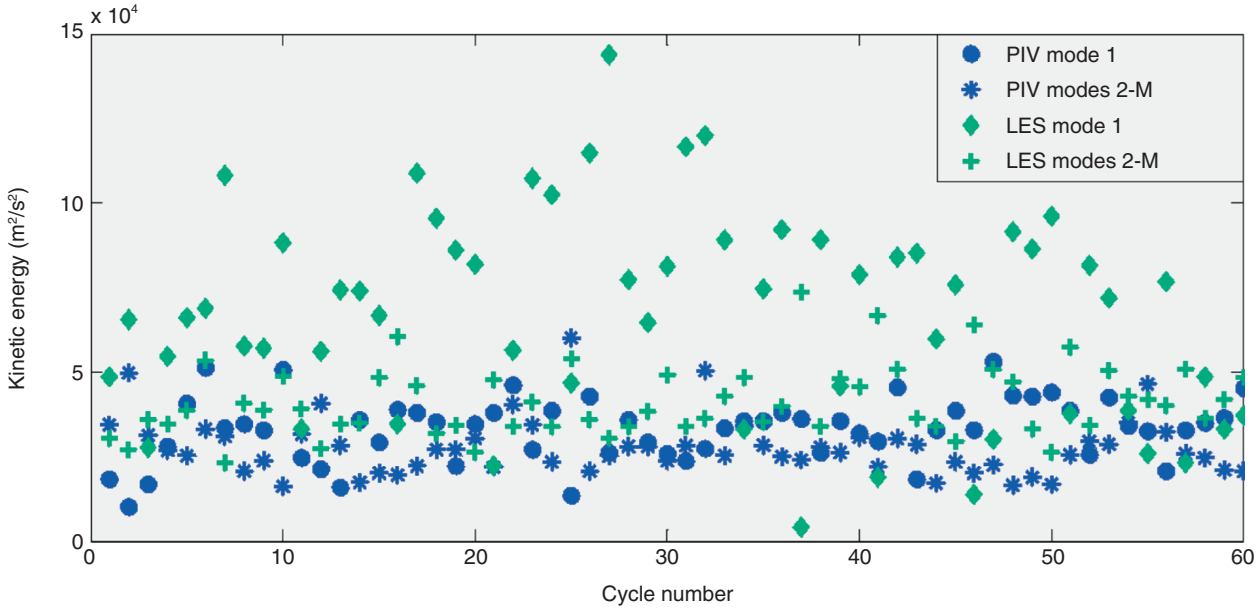

Figure 5

Cyclic variability of PIV and LES RANS average and turbulence energies using phase-dependent POD.

TABLE 4

Metrics used to determine if POD modes may be used to estimate the RANS decomposition applied at 76° ATDCE

RANS Decomposition		Phase-dependent POD, combined cycles
PIV, $KE_{<V>}$ = 33 471 m²/s²	RI = -0.9174	PIV, KE_{m1} = 28 144 m²/s²
PIV, KE_{rms} = 28 648 m²/s²		PIV, $KE_{m2\rightarrow M}$ = 32 660 m²/s²
LES, $KE_{<V>}$ = 63 422 m²/s²	RI = -0.9877	LES, KE_{m1} = 65 001 m²/s²
LES, KE_{rms} = 45 631 m²/s²		LES, $KE_{m2\rightarrow M}$ = 43 291 m²/s²

RI = 0.8532

associated with modes 2 through M is also a good estimate of the RMS velocities. Thus as in Section 3.1.2, the cyclic variability of the ensemble average and turbulence can be quantified but now the energies can be compared between the LES and PIV directly since they use the same set of modes.

For this comparison Figure 6 contains histograms with the total snapshot kinetic energy distribution and the kinetic energy contributions of mode 1 and modes 2 through M to both the PIV and LES data sets at 76° ATDCE and 330° ATDCE. The total snapshot kinetic energy distributions of the PIV and LES data at 76° ATDCE show that the LES data exhibits both larger cyclic variability and higher snapshot kinetic energies than the PIV data. The kinetic energy contributions of mode 1 (an estimate of the contribution of the combined data set ensemble average) to the two data sets at this crank angle show that the PIV data set has both lower cyclic variability and lower kinetic energy contributions from the ensemble average. However, the kinetic energy contributions of modes 2 through M (an estimate of the RANS turbulence) to the two data sets show considerable overlap, although many PIV snapshots have lower turbulence levels than any of the LES snapshots. The PIV data set has ensemble average and RANS turbulence kinetic energy estimates of similar magnitudes and cyclic variability, confirming the conclusions in the previous section. However, the LES data set's ensemble average kinetic energy estimates show

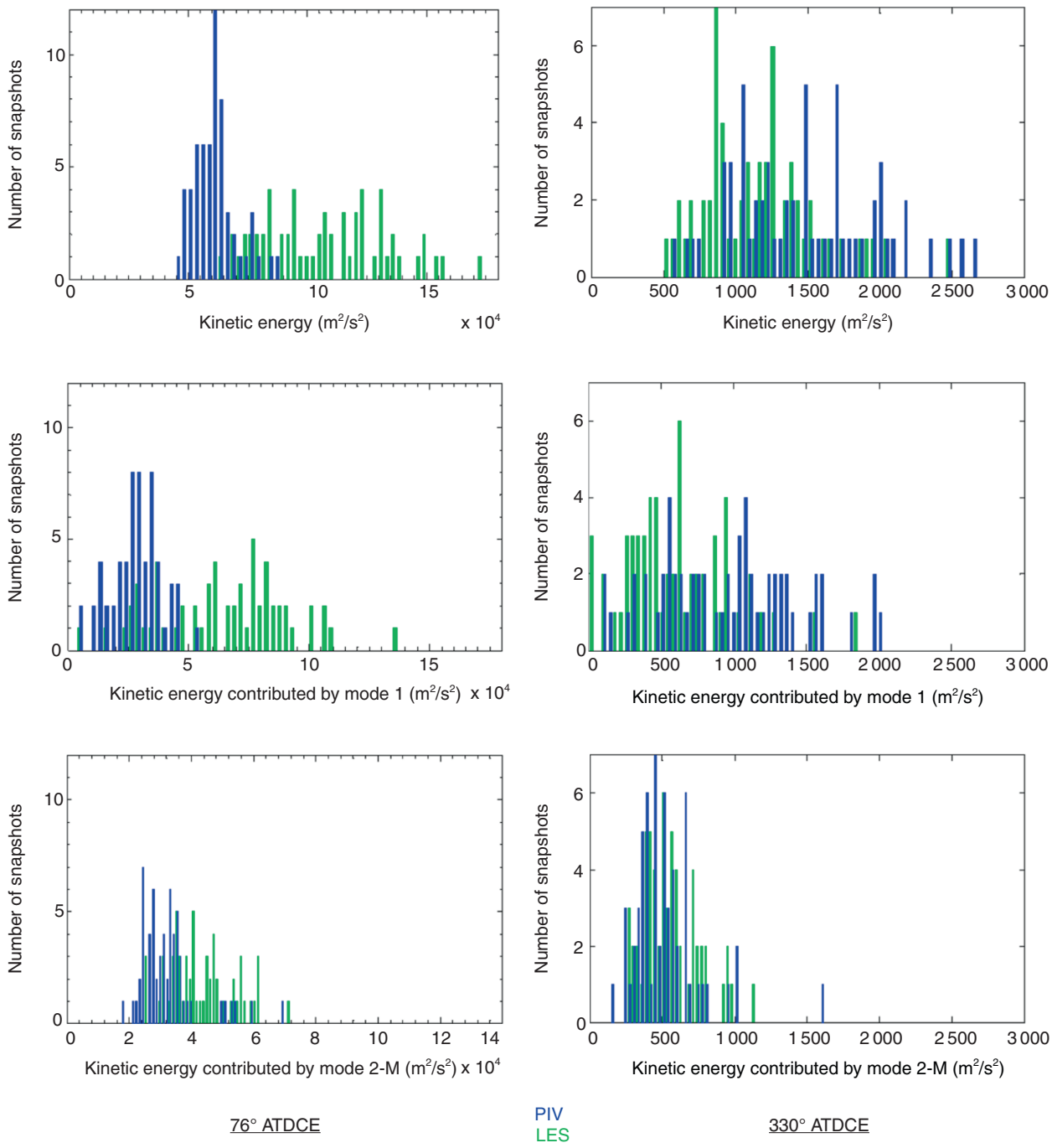

Figure 6

Histograms of total energy in each snapshot (top), of the RANS average energy estimated from phase-dependent POD Mode1 (middle) and RANS turbulence estimated from phase-dependent POD modes 2-M (bottom) at 76° and 330° ATDCE.

greater magnitudes and cyclic variability than the RANS turbulence estimates.

At 330° ATDCE, the histograms of the total snapshot kinetic energies of both the PIV and LES data sets are more similar than at 76° ATDCE, although the PIV data shows somewhat larger cyclic variability and magnitudes. This is also true for the mode 1 kinetic energy contributions. The modes 2 through M kinetic energy

contribution histograms of both data sets also overlap significantly.

3.4 Phase-Invariant POD

While phase-dependent POD is used to analyze velocity data at a particular crank angle, phase-invariant POD analysis provides the hope to both reveal flow-structure evolution similarity through the cycle, as well as to correlate flow events early in the cycle with events late in the cycle. The following section presents the results obtained when phase-invariant POD is performed on a combined PIV and LES data set with two different energy transformation schemes.

Phase-invariant POD requires that all snapshots be analyzed on the same grid. Thus, the PIV data and the interpolated LES data underwent a spatial transformation as their grid were stretched or compressed to match that at engine midstroke. Velocity data from adjacent rows was interpolated using a Gaussian weighting scheme to form new rows of data to fill out stretched grids or to replace two rows with one to fit compressed grids. Changing the number of grid nodes during these spatial transformations changes the mass-specific kinetic energy of the snapshots, but also accounts for the charge density differences between different crank angles. After the spatial transformations, two different energy transformations were considered here.

The unity energy normalization results in each snapshot having a mass-specific kinetic energy of one. In a spatially transformed snapshot k, each velocity vector $\mathbf{V}_{i,j,s.t.}$ (the indices i and j define the location of the vector in the measurement plane and $s,t.$ refers to the spatial transformation) was normalized as follows:

$$V_{i,j,unity\,norm.} = \frac{V_{i,j,s.t.}}{\sqrt{\sum_i \sum_j \left(\frac{1}{2} V_{i,j,s.t.}^2\right)}} \tag{4}$$

Therefore, the flow structures in the snapshots will be distributed among the POD modes based on normalized flow patterns, and each snapshot (cycle) of each crank angle gets equal weighting [7].

The conserved energy transformation results in each snapshot having the same kinetic energy as it did prior to spatial transformation:

$$V_{i,j,conserved\,k.e.} = \frac{V_{i,j,s.t.}}{\sqrt{\sum_i \sum_j \left(\frac{1}{2} V_{i,j,s.t.}^2\right)}} \left(\sqrt{\sum_i \sum_j \frac{1}{2} V_{i,j}^2}\right) \tag{5}$$

The phase-invariant POD was performed on the resultant normalized energy and conserved energy data sets, each containing 60 cycles each of PIV and LES data every 2° from 2° to 360° ATDCE. Figure 7 shows the first three modes obtained for each of the two energy transformations. In the case of using normalized transformation the very high kinetic energy snapshots during intake stroke will have equal energy weighting with snapshots late in the compression stroke, where the kinetic energy has been greatly dissipated (*Fig. 2*). Intuitively, normalization is expected to better retain flow-evolution similarity, since only the flow pattern and not the velocity magnitude is retained. This is demonstrated in Figure 7. The first mode from the normalized energy data set contains aspects of the large-scale tumble vortex present in this engine during the compression stroke, whereas the high-energy jet through the valve during the intake stroke shows in mode 3. Thus, phase-invariant POD of the normalized snapshots set results in dominant modes that best illustrate the evolution of the most repeated velocity structures in the crank angle range examined.

Performing phase-invariant POD using conserved energy snapshots means the flow-structures during the high-energy intake stroke will dominate the lower order modes and the late compression snapshots will be captured in higher order modes. This, too, is demonstrated in Figure 7, where the intake jet flow is now in mode 1 (compared to mode 3 of the normalized transformation) along with two entrainment vortices. Interestingly, these two entrainment vortices were not apparent in either the ensemble average or mode 1 of the phase-dependent analyses. The large-scale tumble dominant in modes 1 and 2 of the normalized analysis is now apparent in modes 2 and 3 of the conserved energy analysis. Thus, it is shown that the two different energy transformations distribute the velocity structures differently between the modes as expected.

Figure 8 shows the distribution and cycle evolution of the coefficients associated with the first three modes of the normalized energy and conserved energy phase-invariant POD analyses. An overarching observation is that the cycle-to-cycle variations are higher, in general, for the LES results for the first three modes over much of the crank angle range that was studied here. However, the normalized mode coefficients in Figure 8 show more similarity between LES and PIV results and each show large values throughout the cycle compared to conserved energy coefficients. Each mode shows elements of flow structures present from different parts of the cycle. This is consistent with the demonstration in [7], that every flow structure in every snapshot is present (to different extents) in every mode. POD on the normalized structures does now not discriminate as much between structures in the intake and compression strokes based on energy, as does the use of the conserved transformation.

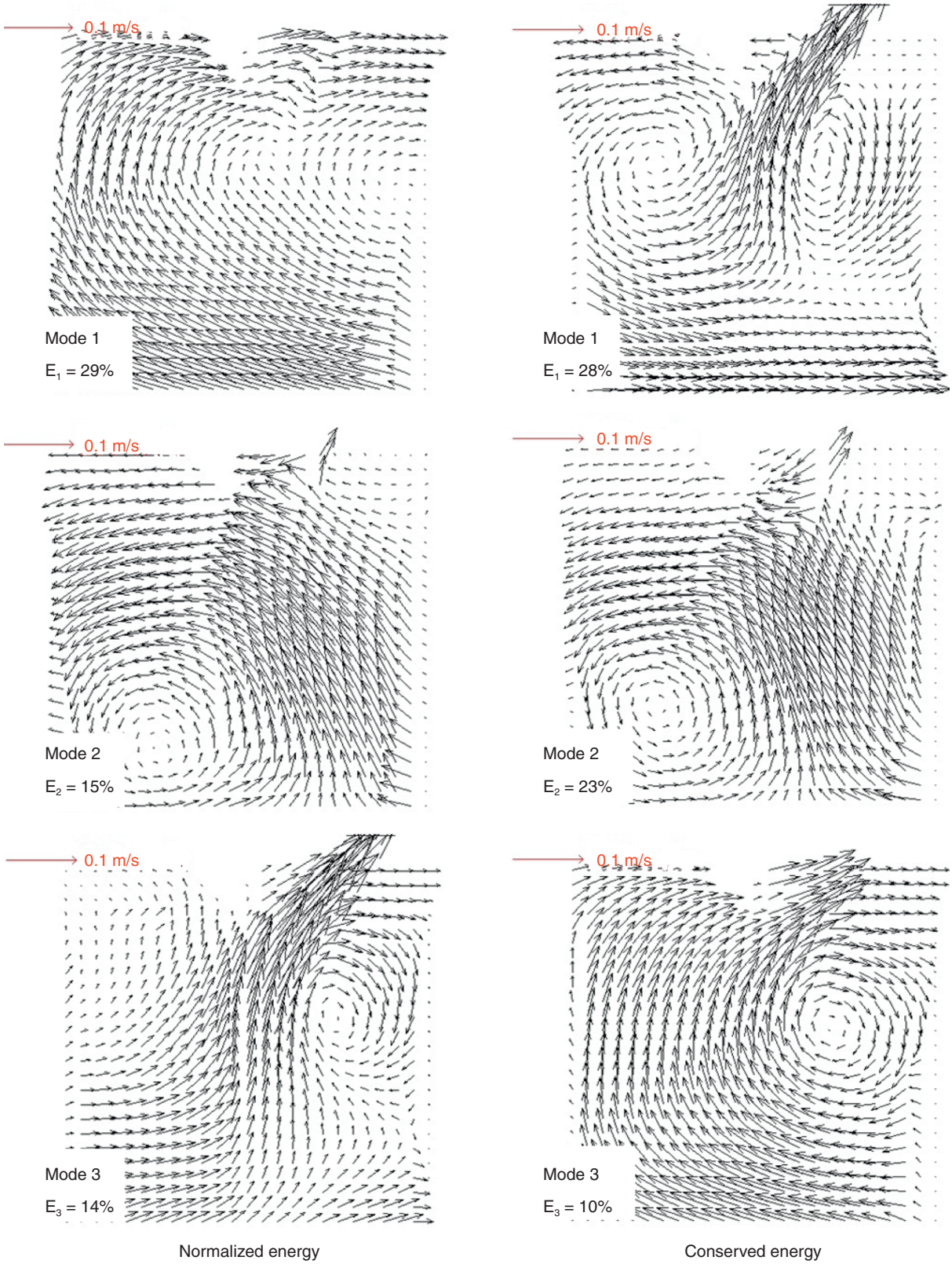

Figure 7

First three modes of phase-invariant POD using each snapshot normalized by its total energy *versus* snapshots which retain (conserve) their total energy.

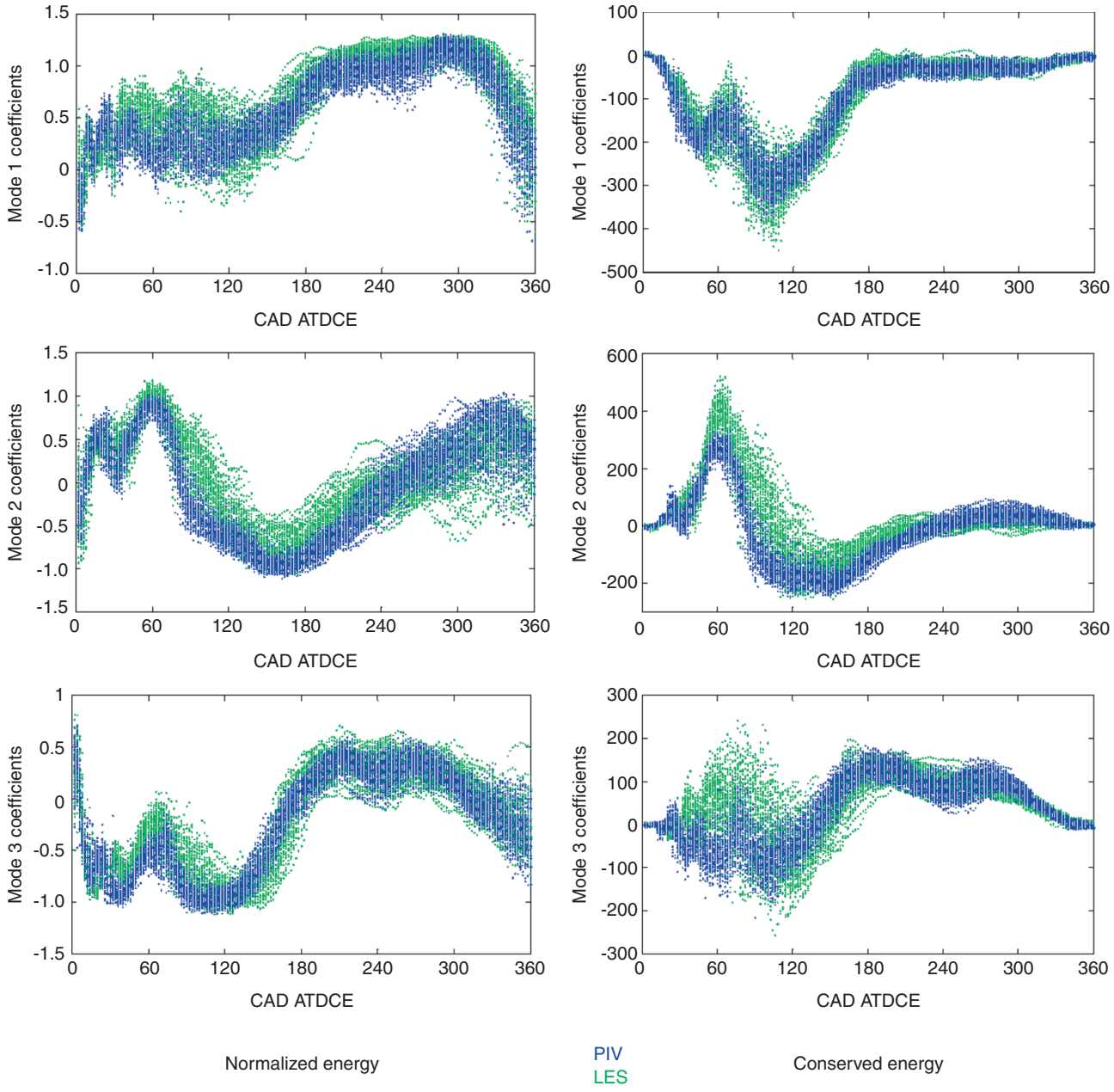

Figure 8

Coefficients of the first three phase-invariant POD modes using each snapshot normalized by its total energy *versus* snapshots which retain (conserve) their total energy.

As discussed earlier, it was expected that the lowest order modes 1 and 2 have high values during the intake and are near zero during the compression stroke (after 180° ATDCE) due to the higher flow velocities during intake that will then dominate the low order modes. The observed high coefficient values of modes 1 and 2 confirm this. The conserved energy mode 3 shows coefficients with large values in both the intake and compression strokes, which suggests there are flow structures with equal energy and repeatability in both strokes. Further, the LES and PIV coefficients differ considerably during the intake stroke. An inspection of the flow pattern in modes 1 and 2 suggests that this may point to slight phasing differences or spatial shifts between LES and PIV for the intake flow jet. Details of this interpretation have yet to be confirmed, though.

These results demonstrate that the use of both normalized energy and conserved energy phase-invariant POD allows for separate examinations of flow structure, flow energy and their evolution. Coefficients from normalized energy phase-invariant POD may be used to study the differences in flow structures and their evolution between any two cycles without also having to account for differences in flow kinetic energy. Proper choice of the normalization approach will help to emphasize certain aspects of the engine cycle that is of particular interest in a specific study. Phase-invariant POD might lead to the identification of cause-and-effect relationships within a cycle or even between cycles: *e.g.*, do particular flow patterns early in the cycle lead to adverse conditions late in the cycle when combustion would be initiated?

CONCLUSION

This paper aims to compare velocity data from an LES model of a single-cylinder motored optical research engine to PIV data obtained from the engine. Two-component PIV data acquired over 60 cycles during the intake and compression strokes and an equal amount of LES velocity data computed under the same operating conditions were compared to each other. The PIV and LES data were compared using ensemble average and RMS velocities and mass-specific kinetic energies. The most significant differences between the data sets were found in sections of the intake stroke, where the kinetic energies of both the ensemble average and RMS velocity fields from the LES data set were larger than that of the PIV data set. Three crank angles were chosen for further examination: 76° ATDCE, during intake jet flow when there were large discrepancies between the PIV and LES ensemble average and RMS velocities, 250° ATDCE, where the ensemble averages show the large-scale tumble vortex present through most of the compression stroke, and 330°, a viable spark timing in a firing engine. Relevance indices were computed to quantify the similarity in terms of velocity structures between the ensemble average velocity fields of the two data sets. For example, the low relevance index at 250° ATDCE is a result of the difference in the location of the center of the large-scale tumble vortex between the two data sets. The low relevance index suggests a difference in flow structures between the PIV and LES data at 250° ATDCE that the spatially summed ensemble average and RMS kinetic energy values did not indicate. Thus, several metrics were required to adequately identify the differences between the PIV and LES data sets.

Unlike more traditional RANS computations, LES computes individual engine cycles and captures cyclic variations. POD was used to compare the PIV and LES data sets as it is a comprehensive comparative analysis and has the potential to estimate the cyclic variability of the ensemble average and RMS flows. Phase-dependent POD was applied separately to the PIV and LES data sets at 76° ATDCE. If, as is the case here, mode 1 is a good estimate of the ensemble average velocity in terms of relevance index and kinetic energy, and modes 2 through M are a good estimate of the RMS velocity, the mass-specific kinetic energy contributions of these modes to individual snapshots may be used to estimate the cyclic variability of the ensemble average and RMS velocities. The separate phase-dependent POD analyses of the data sets indicated that at 76° ATDCE the cyclic variability of the ensemble average of the LES data set was significantly larger than that of the PIV data set and the cyclic variability of the RMS of both data sets were comparable. However, different modes are generated by separate analyses of the PIV and LES data making it impossible to directly and quantitatively compare the data sets using the coefficients. Thus, phase-dependent POD was applied to combined data set of both the PIV and LES velocity fields at 76° ATDCE and 330° ATDCE, resulting in common sets of modes, allowing for a quantitative comparison of the two data sets using just the coefficients. The behavior of the kinetic energy contribution of the modes at 76° ATDCE was similar to that observed using the separate phase-dependent POD analyses. At 330° ATDCE, both data sets were more similar, although the PIV ensemble average and RMS velocities showed more cyclic variability. These results demonstrate how phase-dependent POD coefficients may be used to study cyclic variability within the context of the traditional RANS velocity decomposition. In particular, when mode 1 from phase-dependent analyses of combined PIV and LES data sets is a good estimate of the ensemble averages of both data sets the mode 1 coefficients may be used to directly and quantitatively compare the contribution of the ensemble averages to individual cycles. Similarly, the coefficients from modes 2 through M may be used to estimate and compare the turbulent kinetic energy in individual cycles.

Phase-invariant POD provides a means of analyzing the evolution and cyclic variability of flow structures in a particular crank angle range. Before performing the phase-invariant POD analysis, velocity fields at different crank angles were spatially transformed so that all data would be on the same grid. This spatial transformation changes the mass-specific kinetic energy associated with particular snapshots. Thus, the velocity fields underwent a further energy transformation. Two different energy transformations were explored: the unity energy normalization in which each velocity field to be analyzed is normalized to have a mass-specific kinetic energy of one, and the conserved energy transformation in which the

mass-specific energy of each velocity field prior to the spatial transformation is restored. Phase-invariant POD analyses performed on the combined PIV and LES data set with different energy transformations may be used to extract information about different aspects of engine flow. While the normalized energy phase-invariant POD focuses on differences in flow structure and evolution between the PIV and LES data sets, the conserved energy phase-invariant POD yields information on mass-specific kinetic energy differences as well. The unity energy normalization resulted in a set of modes in which the most persistent flow structure, the large-scale tumble vortex in the compression stroke, dominated and the conserved energy transformation resulted in a set of modes in which the most energetic flow structure, the intake jet flow, dominated. The increases and decreases in the coefficients as a function of crank angle showed the evolution of various flow patterns and the spread in the coefficients indicated cyclic flow variability. These characteristics of phase-invariant POD coefficients may be used to obtain insight into intra-cycle flow correlations. In combination with crank-angle resolved pressure data from the intake system, phase-invariant POD may be used to study the relatively large differences in ensemble average velocities and cyclic flow variability between the PIV and LES data sets.

This study demonstrated the use of different metrics for a more complete understanding of the differences between in-cylinder flow velocity data obtained using PIV and LES. Each metric quantifies different aspects of the flow differences, and it is advisable to use all of them for comprehensive comparisons.

ACKNOWLEDGMENTS

The work conducted at the University of Michigan was sponsored by General Motors through the Engine Systems Research Laboratory of the General Motors Collaborative Research Laboratory. Liu and Haworth gratefully acknowledge financial support from *CD-adapco* and from the *GM R&D Center*. Haworth is a consultant to *CD-adapco*.

REFERENCES

1 Amelio M., Bova S., De Bartolo C. (2000) The Separation Between Turbulence and Mean Flow in ICE LDV Data: The Complementary Point-of-view of Different Investigation Tools, *J. Eng. Gas Turbine. Power* **122**, 579-587.

2 Li Y., Zhao H., Leach B., Ma T., Ladommatos N. (2004) Characterization of an in-cylinder flow structure in a high-tumble spark ignition engine, *Int. J. Engine Res.* **5**, 5, 375-400.

3 St. Hill N., Asadamongkon P., Lee K.C. (2000) A study of turbulence and cyclic variation levels in internal combustion engine cylinders, *Proceedings of the 10th International Symposium on Application of Laser Techniques to Fluid Mechanics*, Lisbon, Portugal, 10-13 July.

4 Jarvis S., Justham T., Clarke A., Garner C.P., Hargrave G. K., Richardson D. (2006) Motored SI IC Engine In-Cylinder Flow Field Measurement Using Time Resolved Digital PIV for Characterisation of Cyclic Variation, *SAE Technical Paper* 2006-01-1044.

5 Baby X., Dupont A., Ahmed A., Deslandes W., Charnay G., Michard M. (2002) A New Methodology to Analyze Cycle-to-Cycle Aerodynamic Variations, *SAE Technical Paper* 2002-01-2837.

6 Cosadia I., Boree J., Charnay G., Dumont P. (2006) Cyclic variations of the swirling flow in a Diesel transparent engine, *Exp. Fluids* **41**, 115-134.

7 Chen H., Reuss D.L., Sick V. (2012) On the use and interpretation of proper orthogonal decomposition of in-cylinder engine flows, *Meas. Sci. Technol.* **23**, 8.

8 Chen H., Reuss D.L., Hung D.L.S., Sick V. (2012) A practical guide for using proper orthogonal decomposition in engine research, *Int. J. Engine Res.*, published online August 31, 2012 as doi: 10.1177/1468087412455748.

9 Fogleman M., Lumley J., Rempfer D., Haworth D. (2004) Application of the proper orthogonal decomposition to datasets of internal combustion engine flows, *J, Turbulence* **5**, 23.

10 Liu K., Haworth D.C. (2011) Development and Assessment of Proper Orthogonal Decomposition for Analysis of Turbulent Flow in Piston Engines, *SAE Technical Paper* 2011-01-0830.

11 Voisine M., Thomas L., Boree J., Rey P. (2011) Spatio-temporal structure and cycle to cycle variations of an in-cylinder tumbling flow, *Exp. Fluids* **50**, 1393-1407.

12 Cosadia I., Boree J., Dumont P. (2007) Coupling time-resolved PIV flow-fields and phase-invariant proper orthogonal decomposition for the description of the parameters space in a transparent Diesel engine, *Exp. Fluids* **43**, 357-370.

13 Haworth D.C. (2005) A review of turbulent combustion modeling for multidimensional in-cylinder CFD, *SAE Technical Paper* 2005-01-0993.

14 Haworth D.C. (1999) Large-eddy simulation of in-cylinder flows, *Oil Gas Sci. Technol.* **54**, 175-185.

15 El Tahry S.H., Haworth D.C. (1992) Directions in turbulence modeling for in-cylinder flows in reciprocating engines, *AIAA J. Propuls. Power* **8**, 1040-1048.

16 Haworth D.C., Jansen K. (2000) Large-eddy simulation on unstructured deforming meshes: Towards reciprocating IC engines, *Comput. Fluids* **29**, 493-524.

17 Celik I.B., Yavuz I., Smirnov A. (2001) Large eddy simulations of in-cylinder turbulence for internal combustion engines: A review, *Int. J. Engine Res.* **2**, 119-148.

18 Celik I.B., Yavuz I., Smirnov A., Smith J., Amin E., Gel A. (2000) Prediction of in-cylinder turbulence for IC engines, *Combust. Sci. Technol.* **153**, 339-368.

19 Celik I.B., Amin E., Smith J., Yavuz I., Gel A. (1998) Towards large eddy simulation using the KIVA- code, *11th International Multidimensional Engine Modeling User's Group Meeting*, Detroit, Michigan, February.

20 Naitoh K., Itoh T., Takagi Y., Kuwahara K. (1992) Large eddy simulation of premixed-flame in engine based on the multi-level formulation and renormalization group theory, *SAE Technical Paper* 920590.

21 Smirnov A., Yavuz I., Celik I.B. (1999) Diesel combustion and LES of in-cylinder turbulence for IC engines, *In-Cylinder Flows and Combustion Processes. ASME Fall Technical Conference*, Ann Arbor, Michigan, October.

22 Smith J., Smirnov A., Yavuz I., Celik I.B. (1998) Simulation of swirling flows related to an intake stroke of a Diesel engine, *ASME ICE-Division Fall Conference*, Clymer, New York, September.

23 Vermorel O., Richard S., Colin O., Angelberger C., Benkenida A. (2007) Multi-cycle LES simulations of flow and combustion in PFI SI 4-valve production engine, *SAE Technical Paper* 2007-01-0151.

24 Richard S., Colin O., Vermorel O., Benkenida A., Angelberger C., Veynante D. (2007) Towards large eddy simulation of combustion in spark ignition engines, *Proc. Combust. Inst.* **31**, 3059-3066.

25 Vermorel O., Richard S., Colin O., Angelberger C., Benkenida A., Veynante D. (2009) Towards the understanding of cyclic variability in a spark ignited engine using multi-cycle LES, *Combust. Flame* **156**, 1525-1541.

26 Laget O., Reveille B., Martinez L., Trun K., Habchi C., Angelberger C. (2011) LES calculations of a four cylinder engine, *SAE Technical Paper* 2011-01-0832.

27 Hu B., Rutland C.J. (2006) Flamelet modeling with LES for Diesel engine simulations, *SAE Technical Paper* 2006-01-0058.

28 Hu B., Jhavar R., Singh S., Reitz R.D., Rutland C.J. (2007) LES modeling of Diesel combustion under partially premixed and non-premixed conditions, *SAE Technical Paper* 2007-01-0163.

29 Hu B., Rutland C.J., Shethaji T. (2008) Combustion modeling of conventional Diesel-type and HCCI type Diesel combustion with LES, *SAE Technical Paper* 2008-01-0958.

30 Enaux B., Granet V., Vermorel O., Lacour C., Thobois L., Dugue V., Poinsot T. (2011) Large Eddy Simulation of a Motored Single-Cylinder Piston Engine: Numerical Strategies and Validation, *Flow Turbul. Combust.* **86**, 153-177.

31 Banerjee S., Liang T., Rutland C.J., Hu B. (2010) Validation of an LES multi-mode combustion model for Diesel combustion, *SAE Technical Paper* 2010-01-0361.

32 Zhang Y., Ghandhi J., Petersen B., Rutland C.J. (2010) Large eddy simulation of scalar dissipation rate in an internal combustion engine, *SAE Technical Paper* 2010-01-0625.

33 Zhang Y., Rutland C.J. (2011) A mixing controlled direct chemistry (MCDC) model for Diesel engine combustion modeling using large-eddy simulation, *Combust. Theory Model.* **16**, 1-18.

34 Rutland C.J. (2011) Large-eddy simulations for internal combustion engines - a review, *Int. J. Engine Res.* **12**, 4, 421-451.

35 Pera C., Angelberger C. (2011) Large Eddy Simulation of a Motored Single-Cylinder Engine Using System Simulation to Define Boundary Conditions: Methodology and Validation, *SAE Technical Paper* 2011-01-0834.

36 Reuss D.L., Rosalik M.E. (1998) PIV Measurements During Combustion in a Reciprocating Internal Combustion Engine, *Proceedings of the 9th International Symposium on Applications of Laser Technologies in Fluid Mechanics*, Lisbon, Portugal, 13-16 July.

37 Reuss D.L. (2000) Cyclic Variability of Large-Scale Turbulent Structures in Directed and Undirected IC Engine Flows, *SAE Technical Paper* 2000-01-0246.

38 Reuss D.L., Kuo T.-W., Khalighi B., Haworth D., Rosalik M. (1995) Particle Image Velocimetry Measurements in a High-Swirl Engine Used for Evaluation of Computational Fluid Dynamics Calculations, *SAE Technical Paper* 952381.

39 Megerle M., Sick V., Reuss D.L. (2002) Measurement of digital particle image velocimetry precision using electro-optically created particle-image displacements, *Meas. Sci. Technol.* **13**, 997-1005.

40 CD-adapco (2011) Methodology for STAR-CD Version 4.16, http://www.cdadapco.com.

41 CD-adapco (2011) User guide for STAR-CD Version 4.16, http://www.cdadapco.com.

42 Asproulis P.N. (1994) High resolution numerical predictions of hypersonic flows on unstructured meshes, *PhD Thesis*, Imperial College, London.

43 Issa R.I. (1986) Solution of the implicitly discretised fluid flow equations by operator-splitting, *J. Comput. Phys.* **62**, 40-65.

44 Issa R.I., Gosman A.D., Watkins A.P. (1986) The computation of compressible and incompressible recirculating flows by a non-iterative implicit scheme, *J. Comput. Phys.* **62**, 66-82.

45 Speziale C.G. (1991) Analytical methods for the development of Reynolds-stress closures in turbulence, *Annu. Rev. Fluid Mech.* **23**, 107-157.

46 Yoshizawa A. (1985) Statistical theory for compressible turbulent shear flows, with the application to subgrid scale modeling, *Phys. Fluids* **29**, 2152-2164.

47 Spalding D.B. (1961) A single formula for the law of the wall, *J. Appl. Mech.* **28**, 455-457.

48 Liu K., Haworth D.C. (2010) Large-eddy simulation for an axisymmetric piston-cylinder assembly with and without swirl, *Flow Turbul. Combust.* **85**, 279-307.

49 CD-adapco (2011) User guide for es-ice Version 4.16, http://www.cdadapco.com.

Manuscript accepted in February 2013
Published online in September 2013